Electronic Supplementary Material (ESI) for Physical Chemistry Chemical Physics.

In situ quasi-elastic neutron scattering study on the water dynamics and reaction mechanisms in alkali-activated slags

Kai Gong[a,b], Yongqiang Cheng[c], Luke L. Daemen[c], Claire E. White[a,b*]
[a] Department of Civil and Environmental Engineering, Princeton University, Princeton NJ 08544, USA
[b] Andlinger Center for Energy and the Environment, Princeton University, Princeton NJ 08544, USA
[c] Chemical and Engineering Materials Division, Oak Ridge National Laboratory, Oak Ridge TN 37830, USA
* Corresponding author: Phone: +1 609 258 6263, Fax: +1 609 258 2799, Email: whitece@princeton.edu
Postal address: Department of Civil and Environmental Engineering, Princeton University, Princeton NJ 08544, USA

Supporting Information

1 Fitting of the quasi-elastic neutron scattering data with a single-Lorentzian model

A single-Lorentzian model,[1, 2] as described by the equation below, has also been used to fit the quasi-elastic neutron scattering (QENS) data:

$$S_{inc}(\omega) = \left\{A\delta(\omega \approx 0) + B_1\left[\frac{\Gamma_1}{\pi({\Gamma_1}^2 + \omega^2)}\right]\right\} \otimes \left[\left(\frac{1}{\sigma\sqrt{2\pi}}\right)e^{(-\omega^2/2\sigma^2)}\right] + (C + D\omega)$$

where the definitions of the parameters in the above equation are the same as the double-Lorentzian model presented in the article. The fitting procedures are also the same as presented in the article except that only three parameters (A, B_1 and Γ_1) are allowed to vary in this case.

The quality of a typical fit using the single-Lorentzian model is compared with that of the double-Lorentzian model in Figure S1a, where it is clearly seen that the double-Lorentzian model results in a better fit to the QENS data. This is further supported by the weighted sum of squared residuals (WSSR) in Figure S1b which shows that the average WSSR for the double-Lorentzian model is at least 2-6 times smaller than that for the single-Lorentzian model for the six types of samples studied. Figure S1b also shows that adding a third Lorentzian (i.e., triple-Lorentzian model as has been used in some previous studies[3, 4]) does not lead to a further reduction in the average WSSR, indicating that the quality of fit could not be further improved with the additional Lorentzian. Due to these results and the fact that a previous QENS study on cementitious materials showed that the double-Lorentzian model is more chemically feasible than the single-Lorentzian model,[1] we decided to use the double-Lorentzian model to fit the QENS data in the article.

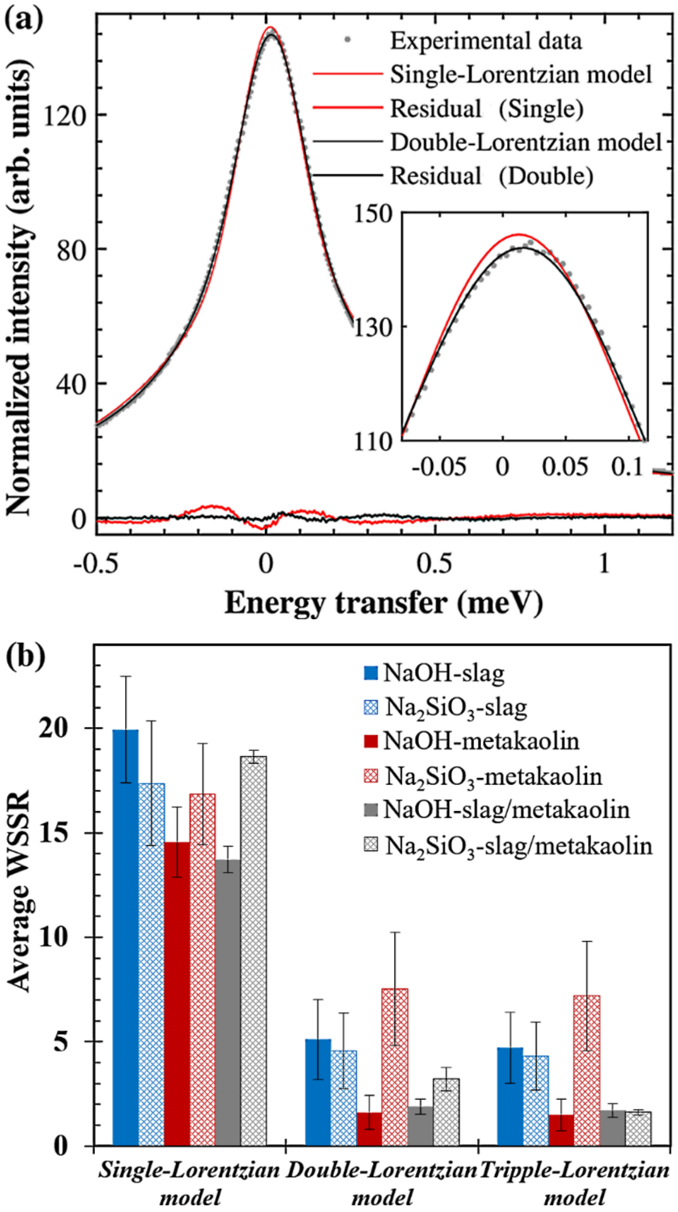

Figure S1. (a) Comparison of the quality of typical fits for a QENS spectrum using single-Lorentzian and double-Lorentzian models. (b) The average weighted sum of squared residuals

(WSSR) from the fitting of single-, double-, and triple-Lorentzian models. The experimental data in (a) is the NaOH-activated slag sample at 1 hour.

2 Inelastic neutron scattering data: Water librational peak

As has been shown in the article, the librational peak of the inelastic neutron scattering (INS) spectra was fitted using three Gaussians, which were then used to calculate the weighted librational peak position (WLPP) parameter. The evolution of the WLPP with the progress of reaction for both NaOH- and Na_2SiO_3-activated slag is illustrated in Figure S2a, while Figure S2b shows the correlations between WLPP and two parameters derived from the analysis of the QENS data: (1) free water index (FWI), and (2) weighted half-width at half-maximum (HWHM) of H/H_2O. The second parameter is determined from the Gaussian and two Lorentzians in the double-Lorentzian model which represents bound, constrained and free water molecules, respectively, using the following equation:

$$\Gamma_{weighted} = \frac{\Gamma_G \cdot A_G + \Gamma_1 \cdot A_{L1} + \Gamma_2 \cdot A_{L2}}{A_G + A_{L1} + A_{L2}}$$

where Γ_G, Γ_1 and Γ_2 are the HWHM of the Gaussian and two Lorentzians, respectively. A_G is the area under the Gaussian, while A_{L1} and A_{L2} are the areas of the two Lorentzians. The $\Gamma_{weighted}$ from the QENS data is a reflection of the average mobility of H/H_2O molecules, with a larger value indicating higher mobility. On the other hand, as explained in the article, WLPP is a reflection of the averaged rotational mobility of water molecules, with a higher WLPP associated with a lower rotational mobility. As a result, an inverse correlation between WLPP and $\Gamma_{weighted}$ is seen in Figure S2b.

Figure S2a clearly shows that the Na_2SiO_3-activated slag exhibits consistently higher WLPP values than the NaOH-activated slag, indicating that the water molecules in the former, on average, have lower rotational mobility. This is in agreement with the $\Gamma_{weighted}$ data in Figure S2b from the QENS analysis, where it is seen that the $\Gamma_{weighted}$ of water molecules is smaller (hence lower mobility) in the Na_2SiO_3- than the NaOH-activated slag sample. This is attributed to the lower FWI in the Na_2SiO_3-activated slag as shown in Figure S2b. In addition, the evolution of the WLPP in Figure S2a suggests that the average rotational mobility of water molecules in the NaOH-activated slag gradually decreases while the Na_2SiO_3-activated slag experiences a slight increase first followed with a slight decrease with the progress of reaction. This initial increase in mobility (decrease in WLPP) is attributed to the increase of FWI in this sample (Figure S9) arising from reduction in Na+Si concentration in the solution via formation of a C-(N)-A-S-H-type gel as already explained in the article. This decrease in WLPP due to an increase of FWI is even more obvious for Na_2SiO_3-activated metakaolin sample (unpublished data) where the Na+Si were taken out of the solution via formation of N-A-S-(H)-type gel. In fact, an inverse correlation is clearly seen between FWI and WLPP as shown in Figure S2b.

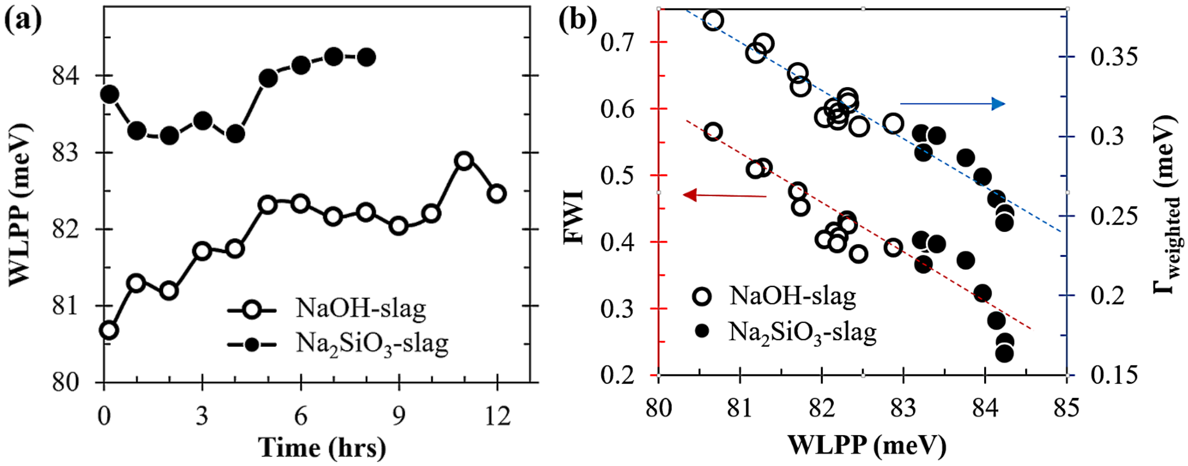

Figure S2. (a) Evolution of the weighted librational peak position (WLPP) for the NaOH- and Na_2SiO_3-activated slags as a function of reaction time, and (b) correlations between WLPP and (i) free water index (FWI) and (ii) the weighted HWHM of the Gaussian and two Lorentzians ($\Gamma_{weighted}$) obtained from fitting the QENS spectra with the double-Lorentzian model. The dashed lines in (b) are provided to guide the eye.

3 Estimating the average number of H_2O molecules solvating each ion in alkaline solutions

The average number of H_2O molecules required to fully solvate a Na^+ ion is around 5.[5] For 1 liter of NaOH solution, there are approximately 55.5 moles of H_2O (1 liter NaOH solution contains approximately 1 liter (or 1000g) H_2O; 1000g/(18g/mol) = 55.5 moles), which is enough to fully solvate the Na^+ ions in the 10 M NaOH solution ($10\times5=50 < 55.5$). For Na_2SiO_3 solutions, the calculation is not as straightforward due to presence of silicate species and their complex speciation in such solutions (the speciation also varies considerably depending on the silicate concentration and Na_2O/SiO_2 of the Na_2SiO_3 solution).[6, 7] Hence, to simplify the calculation here, it is assumed that all the silicate species in the Na_2SiO_3 solutions are silicate monomers in the form of $SiO_2(OH)_2^{2-}$,[8] and each silicate monomer has a hydration number of 5 when fully solvated (according to DFT calculation from our unpublished work). This means that to fully hydrate the Na^+ ions and silicate species in the 2.8 M Na_2SiO_3 solution, the amount of H_2O molecules required is about 42 M ($2.8\times2\times5+2.8\times5=42 < 55.5$), suggesting that there is sufficient water to fully hydrate the Na^+ ions and silicate species in this solution. However, this value becomes 61.5 M ($4.1\times2\times5+4.1\times5=61.5 > 55.5$) and 70.0 M ($5.0\times2\times5+5.0\times4=70.0 > 55.5$) for the 4.1 and 5 M Na_2SiO_3 solutions, respectively, which means that the amount of water in these solutions is not enough to fully hydrate the Na^+ ions and silicate species. Hence some water molecules may be associated with multiple Na^+ ions and/or silicate species at the same time, leading to a further reduction in their mobility. This will result in a transformation of constrained water index (CWI) to bound water index (BWI) for the high concentration Na_2SiO_3 solutions (i.e., 4.1 and 5 M) as seen in Figures 6a and 6b of the article.

4 Isothermal conduction calorimetry (ICC) data for a metakaolin-water mixture

To further illustrate that the initial peak (within ~10 mins after mixing) in the ICC heat flow curves for the alkali-activated slags (see Figure 7 in the manuscript) is dominated by wetting of particle surfaces, ICC heat flow data for a metakaolin-water mixture is provided in Figure S3. Similar to the slag-water mixture, the metakaolin-water mixture also exhibits an intense initial heat flow peak within ~10 mins after mixing. Since it is known that metakaolin dissolution in water is minimal,[9] this initial heat flow peak seen in Figure S3 can only be attributed to the wetting of metakaolin particle surfaces. Figure S3 also shows that the peak heat flow for the metakaolin-water mixture (~34 mW/g) is higher than that of the slag-water mixture (~28 mW/g; Figure 7b), which could be attributed to the larger specific surface area of metakaolin as compared with slag.[10]

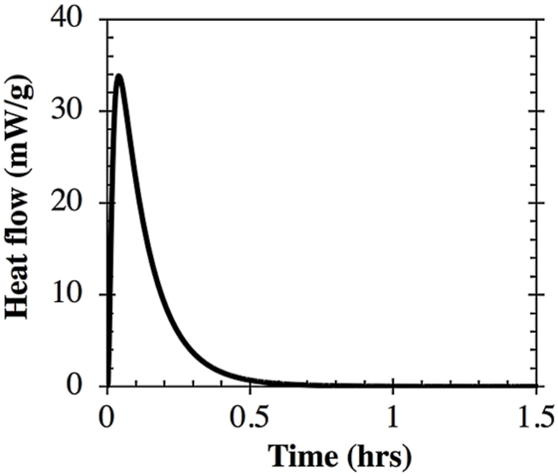

Figure S3. Heat flow curve for a metakaolin-water mixture measured using ICC. This mixture (5 g in total) has a water/metakaolin ratio of 0.9.

5 BWI/CWI/FWI versus cumulative heat for NaOH-activated slag – Initial 2.5 hours

The linear correlations between the BWI/CWI/FWI and ICC cumulative heat are further illustrated in Figure S4, which is a zoomed plot of the initial 2.5 hours of Figure 8b in the article.

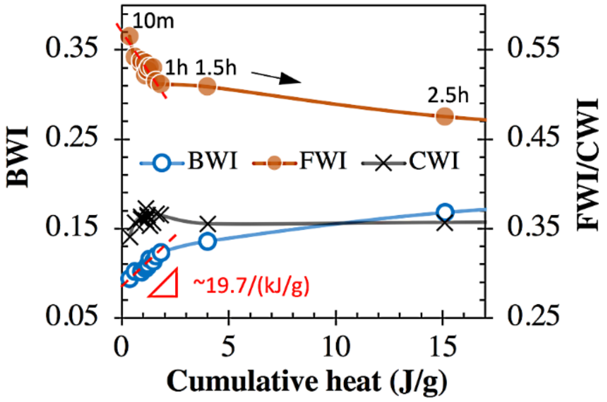

Figure S4. Correlations between ICC cumulative heat and bound water index (BWI)/constrained water index (CWI)/free water index (FWI) for the NaOH-activated slag sample during the initial 2.5 hours.

6 Analysis of the FTIR data for NaOH-activated slag

Detailed analysis of the FTIR spectra for NaOH-activated slag from ~2 to ~12 hours of the activation reaction has been performed by fitting the main v_{as} Si−O−T bands at 700-1100 cm^{-1} with multiple Gaussians and an unreacted slag component, as illustrated in Figure S5. As already discussed in the article, the four Gaussians centered at ~985, ~930, ~895 and ~805 cm^{-1}, can be assigned to asymmetric Si−O stretching in the C-(N)-A-S-H gel associated with different neighboring environments. The contribution from the unreacted slag is determined by scaling the v_{as} Si−O−T band of the neat slag such that the spectrum at ~840-860 cm^{-1} overlap with that of the NaOH-activated slag, as highlighted by the red dashed circle in Figure S5. This is because from Figure 8c in the article we can clearly see that the shoulders at ~840-860 cm^{-1} in the FTIR spectra of the NaOH-activated slag are due to unreacted slag.

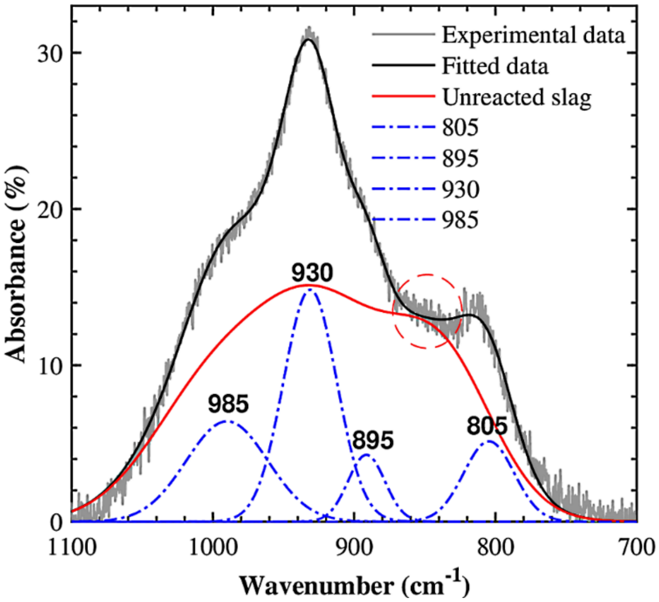

Figure S5. Deconvolution of the FTIR spectrum for NaOH-activated slag at ~12 hours between 700 and 1100 cm^{-1} using multiple Gaussians and the FTIR spectrum of neat slag. The red dashed circle highlights the shoulder at ~840-860 cm^{-1} on the spectrum for NaOH-activated slag which is attributed to unreacted slag in the sample.

Based on the deconvolution of the FTIR spectrum (Figure S5), we have estimated the relative amount of each band in the sample, r_i, using the equation below:

$$r_i = \frac{A_i}{A_s + \sum A_i}$$

where A_i is the area of the i^{th} Gaussian and A_s is the area under the unreacted slag in Figure S5. By plotting r_i of the NaOH-activated slag at different reaction times (from 2 to 12 hours) against the corresponding BWI and FWI obtained from QENS analysis (QENS data are shown in Figure 8b of the article) it is seen that r_i, especially the main band at 930 cm^{-1}, is directly proportional to the BWI (Figure S6) while an inverse correlation with FWI is evident. Given that all the four Si−O stretching bands are attributed to C-(N)-A-S-H gel, as explained in the manuscript, the correlations in Figure S6 clearly demonstrate that precipitation of C-(N)-A-S-H gel is the main factor responsible for the linear conversion of FWI to BWI after ~2.5 hours as seen in Figure 8b of the article.

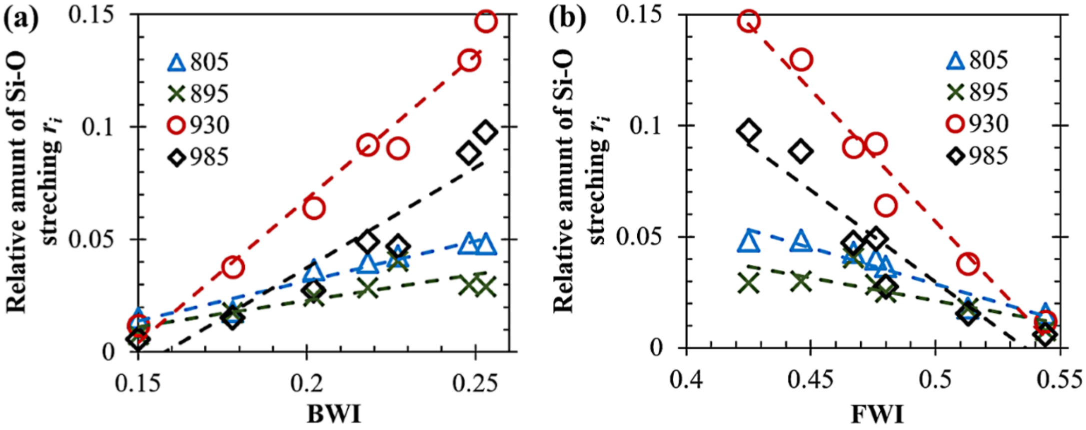

Figure S6. Correlations between the relative amount of Si-O stretching r_i at ~985, ~930, ~895 and ~805 cm^{-1} and (a) bound water index (BWI) and (b) free water index (FWI) derived from QENS analysis. The dashed lines are provided to guide the eye.

7 Surface area and hydrotalcite formation during the initial hour of reaction in the NaOH-activated slag and their potential impacts on BWI

It has been widely reported that an increase of surface area during leaching/dissolution of minerals occurs due to the development of etch pits and incongruent dissolution (including those in cements, e.g., tricalcium silicate).[11-13] The likelihood of forming and growing etch pits in glassy materials during dissolution (e.g., slag) is low due to the lack of structural order, while incongruent dissolution is possible but dependent on a number of factors. For instance, it has been reported that leaching of slag at a constant pH of 7.5 leads to formation of a porous silica-rich surface layer on the partially-dissolved slag particles (due to Ca leaching), which results in an almost fourfold increase in BET specific surface area (from 1.13 to 5.42 m^2/g).[14] However, this dissolution condition is different from that in a highly concentrated alkaline solution (i.e., NaOH), where the solubility of silica and alumina is significantly higher than at neutral pH.[9] Hence, it is difficult to discern if the surface area increases or decreases during the initial hour of reaction, and therefore it is impossible at present to evaluate the impact of changes in surface area on BWI.

The rapid formation of the hydrotalcite-like phase in NaOH-activated slag has been reported in an *in situ* XRD study[15] and thermodynamic modeling[16]. One difference between these two studies is that the XRD study showed that the formation of hydrotalcite-like phase during the initial stage of reaction (before the main ICC reaction peak) is even more pronounced than the formation of the main binder gel (i.e., C-(N)-A-S-H). This pronounced behavior is likely valid for the NaOH-activated slag studied here, due to the high concentration of Mg in the raw slag (14.3 wt. % MgO). In fact, FTIR data in Figure S7 show the emergence of a C−O stretching band at ~1400 cm^{-1} in the NaOH-activated slag immediately after mixing (at ~20 min), which can tentatively be assigned to the hydrotalcite-like phase. To roughly estimate the contribution from hydrotalcite-like phase formation to the increase of BWI during the initial hour as seen in Figure 8b (as compared with the contribution from slag silicate dissolution), we take the slag leaching data in a 5M NaOH solution (similar concentration to what is used here)[17], which showed that the leached Si/Al ratio after 1 hour is about 7:1. Since the dominate silicate species in a 5M NaOH (pH > 14) is $SiO_2(OH)_2^{2-}$,[8] the silicate dissolution and hydrotalcite formation can be simplified as follows:

(1) Silicate dissolution: $SiO_2 + 2\,OH^- \rightarrow SiO_2(OH)_2^{2-}$

(2) Formation of hydrotalcite: $6MgO + Al_2O_3 + CO_2 + 12\,H_2O \rightarrow Mg_6Al_2CO_3(OH)_{16} \cdot 4H_2O$

Reaction (1) generate 2 moles of bound-H atoms per mole of $SiO_2(OH)_2^{2-}$ formed, whereas reaction (2) generate 12 moles of bound-H atoms per mole of Al consumed, assuming most of the leached Al ends up in hydrotalcite and the amount remaining in the solution is relatively small (as shown to be case in NaOH-activated slag[16]). These simple calculations suggest that the contribution to BWI from slag silicate dissolution (2 moles/mole ×7 = 14) and hydrotalcite formation (12 moles/mole ×1 = 12) are comparable (7:6) during the initial hour. The actual ratio for the current sample could be very different because of (1) the differences in dissolution condition, slag chemistry and particle size distribution between the leaching tests in ref. [17] and the NaOH-activated slag studied here, which could influence the ratio of the overall dissolved Si/Al during the initial hour, (2) simplification of the reactions, and (3) several assumptions made (e.g., all the dissolved Al end up in hydrotalcite). Nevertheless, it is reasonable to suggest that the formation of the hydrotalcite-like phase could have a large contribution to the BWI increase in the NaOH-activated slag during the initial hour as seen in Figure 8 of the article.

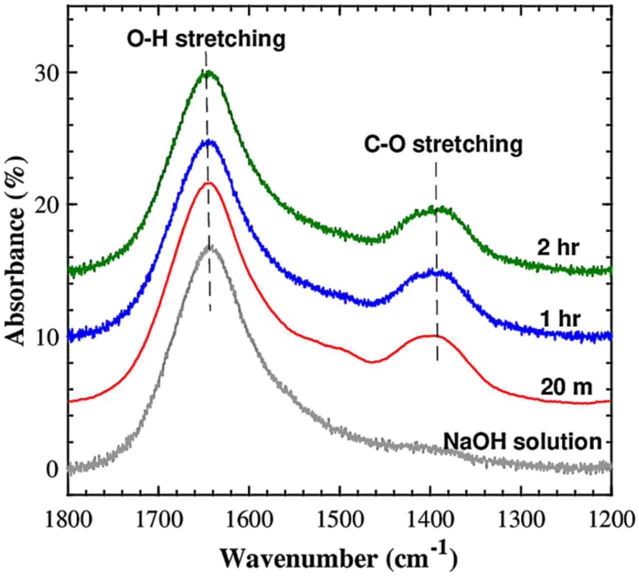

Figure S7. Stacked plot of the FTIR spectra for NaOH-activated slag during the initial two hours between 1200 and 1800 cm^{-1}. Data for the neat NaOH solution are also provided for comparison.

8 Determination of the enthalpy of generating bound H-atoms

In the case of NaOH-activated slag, the total amount of H-atoms (in mole) per gram of paste n_H is calculated:

$$n_H = \frac{W_{water}}{W_{water} + W_{slag} + W_{Na_2O}} \times \frac{1\ mole}{18\ g} \times 2 = \frac{40\ g}{(40 + 100 + 7)\ g} \times \frac{2\ mole}{18\ g} = 0.03\ mole/g$$

where W_{water}, W_{slag} and W_{Na_2O} are the weight of water, slag and Na_2O contained in the alkali-activated slag sample, respectively.

The enthalpy of generating 1 mole of bound H-atoms (H_{BWI}) can be calculated as:

$$H_{BWI} = -\frac{\Delta H_{cumulative\ heat}}{n_H \cdot \Delta BWI} = -\frac{1}{0.03\ mole/g \cdot Slope\ of\ BWI\ vs.Cumulative\ heat\ curve}$$

where $\Delta H_{cumulative\ heat}$ and ΔBWI are the difference in cumulative heat and BWI between two selected reaction times, respectively.

A negative sign is given in the above equation because the reaction is exothermic. The slopes of the BWI vs cumulative heat curve in Figure 8b of the article are ~19.7/(kJ/g) for the initial hour and ~1.6/(kJ/g) after ~2.5 hours. Substituting the slopes into the above equation gives a H_{BWI} of ~ –1.7 and ~ –20.8 kJ/mol, respectively. The enthalpy of generating bound H-atoms for the Na_2SiO_3-activated slag sample has also been calculated following the same procedures, and the results are summarized in Table 2 of the article.

Furthermore, we have also estimated the enthalpy of generating bound H-atoms for different dissolution and precipitation reactions based on thermodynamic data,[18] where the enthalpy of each reaction H_R is determined based on the enthalpy of formation of each constituents, as illustrated below:

$$H_R = \sum_{Products} H_F - \sum_{Reactants} H_F$$

where H_F is the enthalpy of formation of each constituent.

For example, the dissolution of amorphous SiO_2 in mild alkaline solution (pH = 10-12) where the dissolved silicate species is dominated by $SiO(OH)_3^-$ [19] can be written as:

$$SiO_2 + H_2O + OH^- = SiO(OH)_3{}^-$$

The enthalpy of above reaction can be calculated as: $H_R = -1430.9$ kJ/mol – (– 903 – 285.9 – 230) kJ/mol = –12 kJ/mol, where the formation energy of each constituents are obtained from ref. [18]. This value is close to what was reported in the literature for dissolution of amorphous SiO_2 in mild alkaline solutions (~ –12.8 kJ/mol).[20] Since each mole of $SiO(OH)_3^-$ formed generates 3 moles of bound H-atoms, the enthalpy of generating bound H-atom via the above reaction is approximately 4 kJ/mol. Similarly, the enthalpy of generating bound H-atom for different reactions are calculated based on ref. [18] and summarized in Table S1 below.

Table S1. Enthalpy of reaction and enthalpy per mole of bound H-atoms generated for different reactions. Note that the reactions in the AAS samples are highly complex and the ones listed below are some of the simplified possible reaction pathways. T5C* is one common type of C-S-H gel structure which has the same chemical composition as T5C but slightly modified thermodynamic properties,[18] and T5C is an ordered pentameric tobermorite-like end member where the interlayer Ca^{2+} occupancy is full.[21]

Reactions	Bound H-atoms per mole of reaction	Enthalpy of reaction H_R (kJ/mole)	Enthalpy per mole of bound H-atoms generated H_{BWI} (kJ/mole)
$SiO_2+H_2O+OH^- \rightarrow SiO(OH)_3^-$	3	–12.0	–4.0
$SiO_2+2H_2O \rightarrow Si(OH)_4$	4	–15.0	–3.8
$SiO_2+2OH^- \rightarrow SiO_2(OH)_2^{2-}$	2	–21.9	–11.0
$Al_2O_3 + 3H_2O+2OH^- \rightarrow 2\ Al(OH)_4^-$	8	–1.1	–0.183
$CaO + H_2O \rightarrow Ca^{2+} + 2\ OH^-$	0	–82.2	N/A
$MgO + H_2O \rightarrow Mg^{2+} + 2\ OH^-$	0	–38.4	N/A
$1.25Ca^{2+} + 1.25\ SiO_2(OH)_2^{2-} + 1.25H_2O \rightarrow 1.25CaO\bullet 1.25SiO_2\bullet 2.5H_2O$ (T5C*)	2.5	–12.6	–5.0
$1.25CaO + 1.25\ SiO_2(OH)_2^{2-} + 2.5H_2O \rightarrow 1.25CaO\bullet 1.25SiO_2\bullet 2.5H_2O$ (T5C*) + $2.5OH^-$	2.5	–92.3	–36.9
$1.25CaO + 1.25SiO_2 + 2.5H_2O \rightarrow 1.25CaO\bullet 1.25SiO_2\bullet 2.5H_2O$ (T5C*)	5	–142.8	–28.6
$6MgO + Al_2O_3 + CO_2 + 12H_2O \rightarrow Mg_6Al_2CO_3(OH)_{16}\bullet 4H_2O$	24	118.2	4.9
$4CaO + Al_2O_3+0.5CO_2 + 11.5H_2O \rightarrow Ca_4Al_2(OH)_{12}[OH(CO_3)_{0.5}]\bullet 5H_2O$	23	–566.2	–24.6

9 BJH pore size distribution from N_2 sorption

Figure S8 shows the pore size distribution and cumulative pore volume for the NaOH- and Na_2SiO_3-activated slag samples at 6 and 12 hours. The pore size distribution is determined based on the BJH adsorption branch of the N_2 sorption analysis as briefly outlined in Section 3.2.4 of the article. The results (Figure S8a) clearly reveal that the pores developed in the NaOH-activated slag are predominately capillary pores (d > 10 nm) and a large proportion of the pores are outside the range of the N_2 measurements (i.e., capillary pores with a diameter greater than ~50 nm). In contrast, for the Na_2SiO_3-activated slag sample, pores of much smaller size (d < ~10 nm) have already developed by 6 hours, with approximately 9% volume of pores measured using N_2 sorption smaller than ~5 nm (Figure S8b), which can be considered as gel pores arising from C-(N)-A-S-H-type gel. After 12 hours, the pore size further decreases significantly, with over 50% volume of pores accessible using N_2 sorption smaller than ~5 nm. Furthermore, the cumulative pore volume in the Na_2SiO_3-activated slag (~0.14 cm^3/g) is seen to be almost twice of that in the NaOH-activated slag (~0.08 cm^3/g), likely due to the presence of a significant portion of large pores (> 50 nm) in the latter that were not accessible using N_2 sorption experiments.

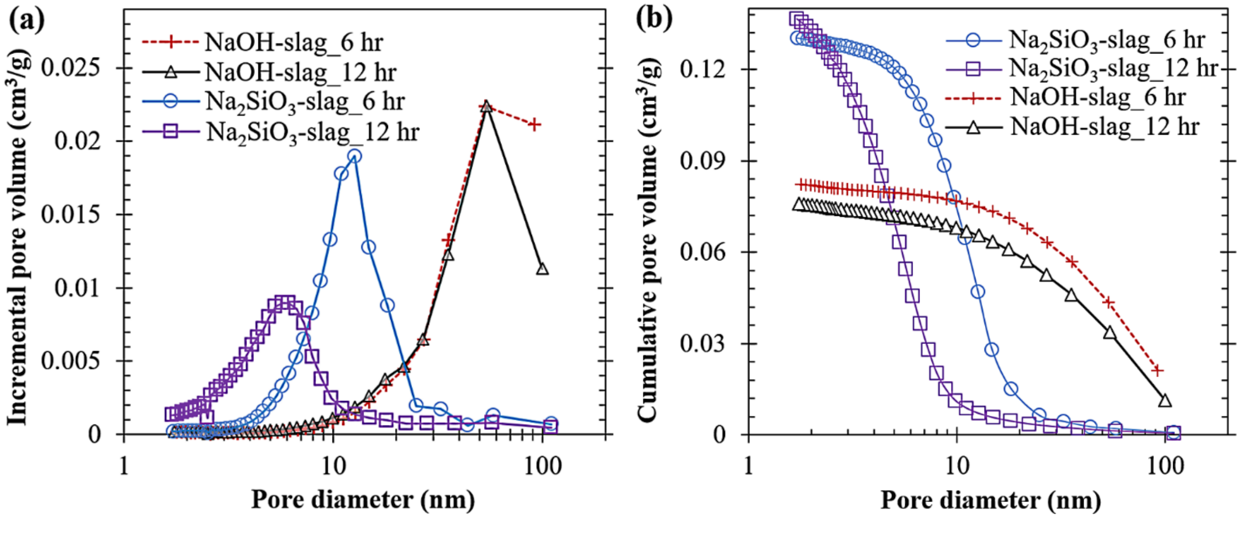

Figure S8. (a) Incremental and (b) cumulative pore size distribution of the NaOH- and Na_2SiO_3-activated slag at 6 and 12 hours obtained using the BJH adsorption branch from N_2 sorption analysis.

10 Evolution of CWI and FWI as a function of time for the Na_2SiO_3-activated slag

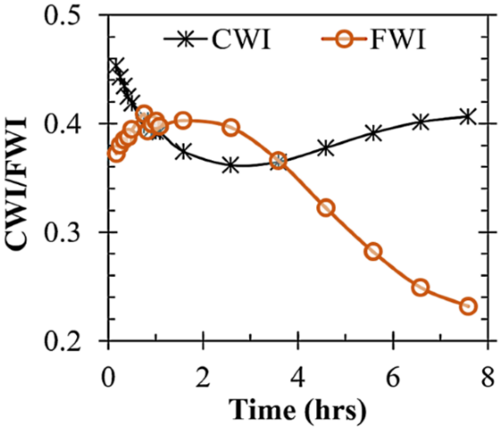

Figure S9. Evolution of constrained water index (CWI) and free water index (FWI) with the progress of reaction for Na_2SiO_3-activated slag.

11 References

1. J. J. Thomas, S. A. FitzGerald, D. A. Neumann and R. A. Livingston, *J. Am. Ceram. Soc.*, 2001, **84**, 1811-1816.
2. S. A. FitzGerald, D. A. Neumann, J. J. Rush, D. P. Bentz and R. A. Livingston, *Chem. Mater.*, 1998, **10**, 397-402.
3. V. K. Peterson, D. A. Neumann and R. A. Livingston, *J. Phys. Chem. B*, 2005, **109**, 14449-14453.
4. V. K. Peterson, D. A. Neumann and R. A. Livingston, *Physica B*, 2006, **385-386**, 481-486.
5. R. W. Impey, P. A. Madden and I. R. McDonald, *J. Phys. Chem.*, 1983, **87**, 5071-5083.
6. L. Vidal, E. Joussein, M. Colas, J. Cornette, J. Sanz, I. Sobrados, J. L. Gelet, J. Absi and S. Rossignol, *Colloid Surface A*, 2016, **503**, 101-109.
7. J. S. Falcone Jr, J. L. Bass, P. H. Krumrine, K. Brensinger and E. R. Schenk, *J. Phys. Chem. A*, 2010, **114**, 2438-2446.
8. J. Šefčík and A. V. McCormick, *AIChE J.*, 1997, **43**, 2773-2784.
9. I. Garcia-Lodeiro, A. Palomo and A. Fernández-Jiménez, in *Handbook of alkali-activated cements, mortars and concretes*, eds. F. Pacheco-Torgal, J. A. Labrincha, C. Leonelli, A. Palomo and P. Chindaprasirt, Woodhead Publishing, Cambridge, UK, 2015, pp. 49-73.
10. S. U. Khan, M. F. Nuruddin, T. Ayub and N. Shafiq, *Scientific World J.*, 2014, **2014**.
11. F. Bellmann, T. Sowoidnich, H.-M. Ludwig and D. Damidot, *Cem. Concr. Res.*, 2015, **72**, 108-116.
12. V. Robin, B. Wild, D. Daval, M. Pollet-Villard, A. Nonat and L. Nicoleau, *Chem. Geol.*, 2018, **497**, 64-73.
13. Z. Hailin, P. R. Bloom and E. A. Nater, *Geochim. Cosmochim. Ac.*, 1993, **57**, 1681-1689.
14. S. N. Lekakh, C. H. Rawlins, D. G. C. Robertson, V. L. Richards and K. D. Peaslee, *Metall. Mater. Trans. B*, 2008, **39**, 125-134.
15. Z. Sun and A. Vollpracht, *Cem. Concr. Res.*, 2018, **103**, 110-122.
16. B. Lothenbach and A. Gruskovnjak, *Adv. Cem. Res.*, 2007, **19**, 81-92.
17. C. K. Yip, G. C. Lukey, J. L. Provis and J. S. J. van Deventer, *Cem. Concr. Res.*, 2008, **38**, 554-564.
18. R. J. Myers, B. Lothenbach, S. A. Bernal and J. L. Provis, *Appl. Geochem.*, 2015, **61**, 233-247.
19. C. E. White, J. L. Provis, G. J. Kearley, D. P. Riley and J. S. J. van Deventer, *Dalton T.*, 2011, **40**, 1348-1355.
20. J. D. Rimer, O. Trofymluk, A. Navrotsky, R. F. Lobo and D. G. Vlachos, *Chem. Mater.*, 2007, **19**, 4189-4197.
21. D. A. Kulik, *Cem. Concr. Res.*, 2011, **41**, 477-495.